

## Article

# Mechanical Properties and Microstructural Evolution of TiNi-Based Intermetallic Alloy with Nb Addition

Hsin-Feng Yang, Tao-Hsing Chen \*  and Ying-Ying Syu

Department of Mechanical Engineering, National Kaohsiung University of Science and Technology, Kaohsiung 80778, Taiwan; yanghf@nkust.edu.tw (H.-F.Y.); stars0619@gmail.com (Y.-Y.S.)

\* Correspondence: thchen@nkust.edu.tw; Tel.: +886-7-3814526

**Abstract:** TiNi intermetallic alloys were prepared with 2, 4 and 6 at.% niobium (Nb) addition. The mechanical properties and microstructures of the alloys were investigated under both static ( $1 \times 10^{-1}$  to  $1 \times 10^{-3} \text{ s}^{-1}$ ) and dynamic ( $4 \times 10^3$  to  $6 \times 10^3 \text{ s}^{-1}$ ) loading conditions. The intermetallic alloy structures and surface morphologies of the alloys were examined by X-ray diffraction (XRD) and scanning electron microscopy (SEM), respectively. In addition, the fracture morphologies were observed by optical microscopy (OM). It was shown that the addition of 2 to 4 at.% Nb increased the strength of the TiNi alloy. However, as the level of Nb addition was further increased to 6 at.%, a significant reduction in strength occurred. For a constant Nb addition, the plastic flow stress and strain rate sensitivity increased with increasing strain rate under both loading conditions (static and dynamic). The XRD and SEM results showed that the original surface morphologies were composed primarily of dendritic structures and fine  $\beta$ -Nb + TiNi eutectic systems. Moreover, the OM results showed that the alloys underwent a transition from a brittle fracture mode to a ductile fracture mode as the level of Nb addition increased.

**Keywords:** TiNi-based intermetallic alloy; universal testing machine; split-Hopkinson pressure bar; mechanical properties



**Citation:** Yang, H.-F.; Chen, T.-H.; Syu, Y.-Y. Mechanical Properties and Microstructural Evolution of TiNi-Based Intermetallic Alloy with Nb Addition. *Materials* **2022**, *15*, 3124. <https://doi.org/10.3390/ma15093124>

Academic Editor: Thomas Niendorf

Received: 29 March 2022

Accepted: 24 April 2022

Published: 26 April 2022

**Publisher's Note:** MDPI stays neutral with regard to jurisdictional claims in published maps and institutional affiliations.



**Copyright:** © 2022 by the authors. Licensee MDPI, Basel, Switzerland. This article is an open access article distributed under the terms and conditions of the Creative Commons Attribution (CC BY) license (<https://creativecommons.org/licenses/by/4.0/>).

## 1. Introduction

Intermetallic compounds (IMCs) consist of two or more metallic or metalloid elements with specific atomic ratios and have an ordered crystalline structure. Such alloys have an attractive combination of physical and mechanical properties, including a high melting point, light weight, high strength, and good oxidation and creep resistance. As a result, they are regarded as promising materials for a wide range of applications in the aerospace, automobile, and nuclear energy fields [1–3]. Many IMCs have been developed in recent decades, including FeAl, Ni<sub>3</sub>Al, TiAl and TiNi [4–10]. Among these alloys, TiNi intermetallic alloys have been used for many practical applications in biomedical and engineering fields due to their excellent performance, such as biocompatibility, anti-corrosion and high mechanical properties and shape memory effect. However, the TiNi alloy was first used for shape memory due to good transform hysteresis [11–13]. TiNi alloy also has a hardness comparable to that of tool steel, and good superelasticity. So, it is one of the most promising alloy systems for bearings, automobiles and related applications [14]. TiNi-based alloys have also found widespread application in fields such as aerospace engineering, intelligent control, and medical implants [15–17]. As with all IMCs, TiNi has good mechanical strength at elevated temperatures; however, it exhibits relatively brittle behavior under ambient temperature conditions, and thus has restricted applicability at lower working temperatures.

The microstructure of TiNi alloy is B2 high temperature matrix phase. The microstructure has super-elasticity and shape memory; this makes TiNi alloys difficult to be machined and to be highly resistant to deformation. These factors are due to diffusionless martensitic

transformation. Over recent decades, many studies have been conducted on the effect of using ternary alloying elements for the improvement of mechanical properties or grain refinement treatment [18,19]. Many studies have shown that the properties of IMCs can be tuned through the addition of carefully chosen doping elements. For example, the addition of hafnium (Hf) reduces the solid solution temperature and is hence advantageous in lowering manufacturing costs at an industrial scale [20,21]. Similarly, the addition of Al induces a grain refinement effect, which is beneficial in enhancing IMC hardness [22,23]. The addition of Nb as a doping element has attracted particular attention due to its effects in enhancing the yield strength through the formation of ultrafine grains, good corrosion resistance at high temperature, and high dislocation density [24–26]. Co-addition is also beneficial in improving the solid solution strengthening effect and magnetic hysteresis, thereby improving the thermal coupling performance and oxidation resistance [27]. During the forming process and application, the TiNi alloy will suffer differential strain rate deformation, so it is necessary to investigate the strain rate effect on the TiNi alloy. Intermetallic alloys can be fabricated through various methods, including casting, powder metallurgy, self-propagation high-temperature synthesis (SHS), directional solidification, selective laser melting, and electron beam melting [28–30]. However, the vacuum arc melting method is easy to operate and a low-cost method. This study used this method to fabricate the experimental specimens.

Some studies have reported that the addition percentage of Nb is high, but will enhance the high yielding strength due to the  $\beta$ -Nb phase composite mechanism [31,32]. However, high yielding strength was also shown to be associated with decreased ductility. It is important to achieve good mechanical properties including both strength and ductility. Accordingly, the present study prepared TiNi alloys with 2, 4 and 6 at.% Nb addition and investigated their mechanical properties and microstructural evolution over a wide strain rate range of  $10^{-3} \text{ s}^{-1}$  to  $6 \times 10^3 \text{ s}^{-1}$ . The effects of the precipitation phase on the mechanical properties of the TiNi-Nb alloys were examined by X-ray diffraction (XRD) and scanning electron microscopy (SEM). Finally, the fracture mechanisms of the various alloys were investigated by observing fracture surfaces using an SEM facility.

## 2. Experimental Procedures

In the present study, TiNi-Nb alloys were prepared in a vacuum arc melting furnace under argon gas. High-purity (99.99%) Ti, Ni and Nb powders were purchased from the Golden Optoelectronic Company (Taipei, Taiwan). The TiNi alloys were prepared using a constant Al content of 44 at.%, Nb contents of 2, 4 or 6 at.%, and a balance of Ti. The  $\text{TiNi}_{44}\text{Nb}_2$ ,  $\text{TiNi}_{44}\text{Nb}_4$  and  $\text{TiNi}_{44}\text{Nb}_6$  ingots were melted at temperatures between 1573 K and 1673 K for 6 h, allowed to cool to room temperature in the furnace, and then reheated once again. To ensure compositional homogeneity, each ingot was remelted five times. Furthermore, to ensure homogenization, the homogenization process was performed keeping the alloys at 1060 °C for 20 h in a vacuum furnace. The as-cast ingots were machined into cylindrical bars with a diameter of 5 mm. and the bars were then cut into test specimens with a length of 5 mm using a low-speed cutter. The phase compositions and microstructures of the three alloys were examined via XRD analysis and SEM (JEM7001, JEOL Ltd., Akishima, Japan). The mechanical characteristics of each specimen were then investigated under room temperature conditions using quasi-static and dynamic tests. In the quasi-static tests, the specimens were deformed at strain rates of  $10^{-3} \text{ s}^{-1}$ ,  $10^{-2} \text{ s}^{-1}$  and  $10^{-1} \text{ s}^{-1}$ , respectively, using a material testing system (MTS Landmark; Sinodynamics Enterprise Co., Ltd., Taipei, Taiwan). The dynamic tests were performed under lubricated conditions using a compression split-Hopkinson pressure bar (SHPB) at strain rates of  $4000 \text{ s}^{-1}$ ,  $5000 \text{ s}^{-1}$  and  $6000 \text{ s}^{-1}$ , respectively. Finally, the fracture surfaces of the specimens were observed by SEM.

### 3. Results and Discussion

#### 3.1. XRD Structural Analysis

XRD analyses were performed to identify the intermetallic alloy structures of the as-cast  $\text{TiNi}_{44}\text{Nb}_2$ ,  $\text{TiNi}_{44}\text{Nb}_4$  and  $\text{TiNi}_{44}\text{Nb}_6$  alloys. The XRD pattern shown in Figure 1a for the  $\text{TiNi}_{44}\text{Nb}_2$  alloy contained prominent peaks corresponding to the TiNi (B2) phase in the (110), (200) and (211) directions, together with several peaks corresponding to  $\text{Ti}_2\text{Ni}$ . As the Nb addition increased to 4 at.%, the intensity of the  $\text{Ti}_2\text{Ni}$  peaks decreased substantially with the peak at  $42^\circ$ – $50^\circ$  disappearing completely. Finally, for 6 at.% Nb addition, a soft  $\beta$ -Nb phase with a BCC crystal structure was newly formed. In other words, the addition of a larger quantity of Nb produced a mixed TiNi (B2) +  $\beta$ Nb phase structure through a eutectic reaction.

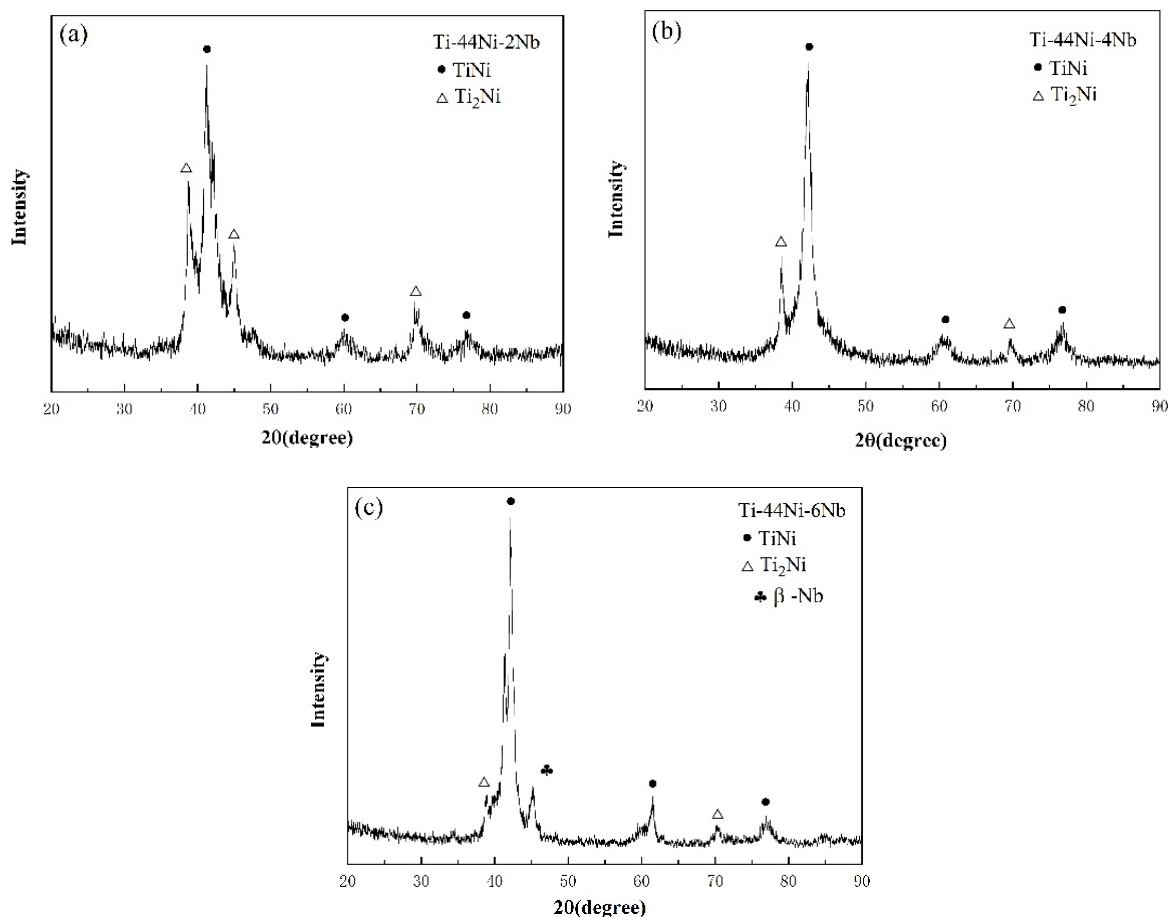


**Figure 1.** XRD patterns of: (a)  $\text{TiNi}_{44}\text{Nb}_2$ , (b)  $\text{TiNi}_{44}\text{Nb}_4$ , and (c)  $\text{TiNi}_{44}\text{Nb}_6$  alloys.

#### 3.2. Surface Morphology Analysis

In order to observe microstructure, all the tested specimens were cold-coated with polyester resin, and then polished. Then, the specimens were etched in chemical solution with a volume ratio of  $\text{HF}:\text{HNO}_3:\text{H}_2\text{O} = 1:1:7$  for 20 s and their microstructures and chemical composition were determined with SEM and EDX systems. Figure 2a–c present SEM surface morphology images of the  $\text{TiNi}_{44}\text{Nb}_2$ ,  $\text{TiNi}_{44}\text{Nb}_4$  and  $\text{TiNi}_{44}\text{Nb}_6$  alloys. It can be seen that all the alloys comprise a dendritic TiNi (B2) substrate with a black  $\text{Ti}_2\text{Ni}$  intermetallic phase. As the level of Nb addition increased, the alloy structure became more refined, and the dendritic structure became denser. As indicated by the XRD analysis results, the  $\text{TiNi}_{44}\text{Nb}_6$  alloy was composed of a dendritic TiNi (B2) matrix together with eutectic structures around the grain boundaries. Figure 2d,e present the EDX analysis for Figure 2a–c, respectively. From the EDX analysis, the microstructure containing Ti, Ni and

Nb elements can be seen. The primary and secondary dendrites for  $\text{TiNiNb}_2$  were about  $40\ \mu\text{m}$  and  $5\ \mu\text{m}$  in size. The primary and secondary dendrites for  $\text{TiNiNb}_4$  were about  $30\ \mu\text{m}$  and  $10\ \mu\text{m}$  in size. The primary dendrites for  $\text{TiNiNb}_6$  were less than  $10\ \mu\text{m}$  and almost disappeared, while the secondary dendrites for  $\text{TiNiNb}_6$  were about  $12\ \mu\text{m}$  and became discontinuous. The precipitate  $\beta\text{-Nb}$  in the matrix can also be seen (Figure 2g is the large magnification figure for Figure 2c). In the literature, it is suggested that as the Nb content increases the temperature of the phase transformation and related mechanical properties will increase [33,34].

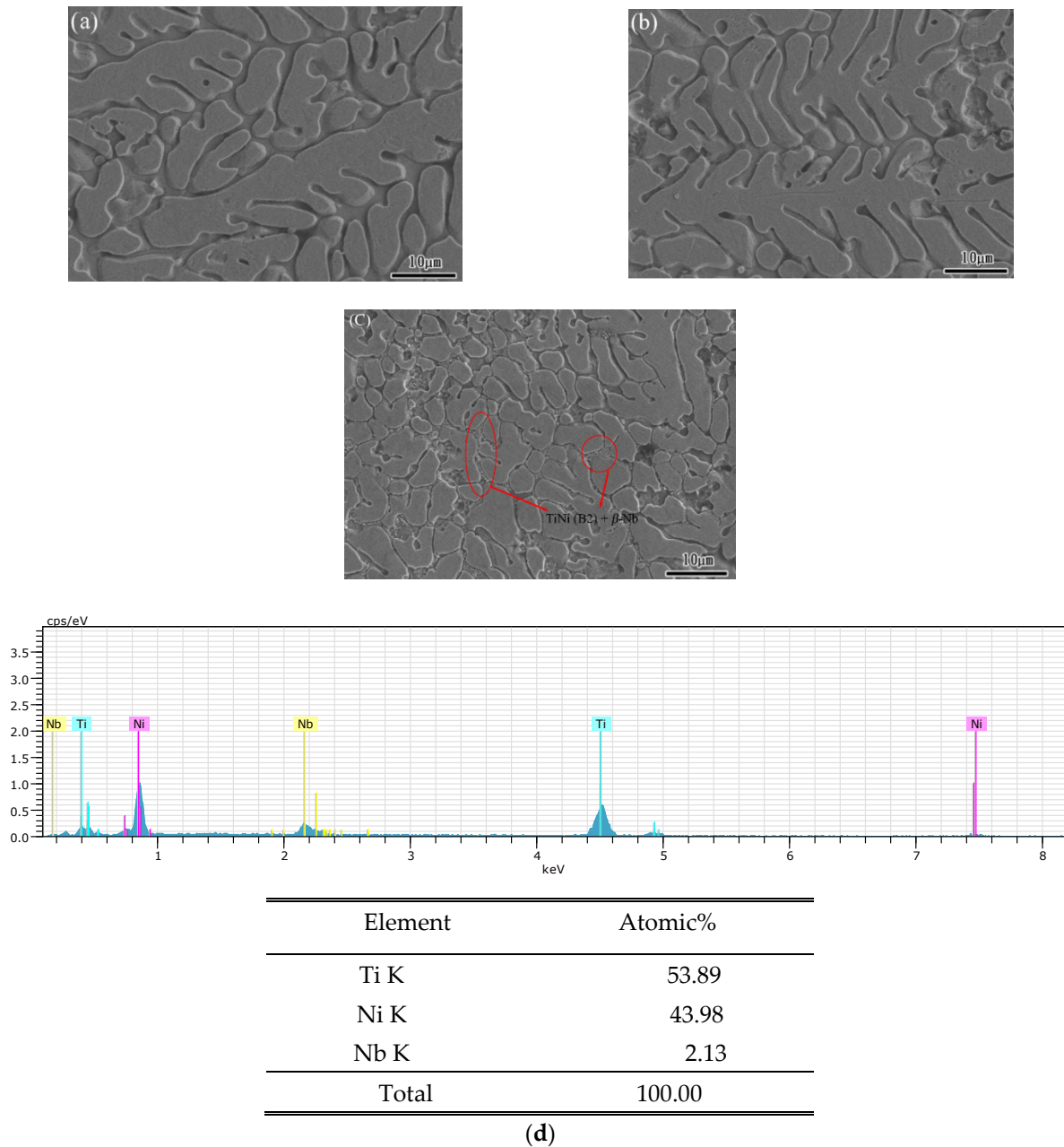
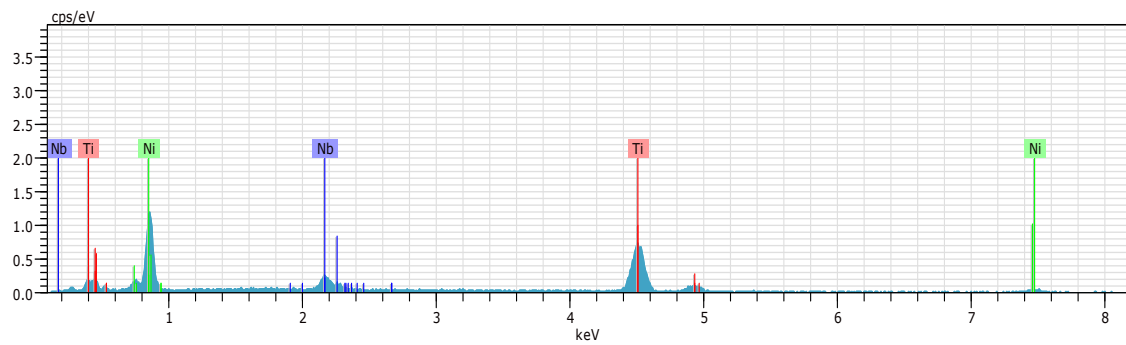
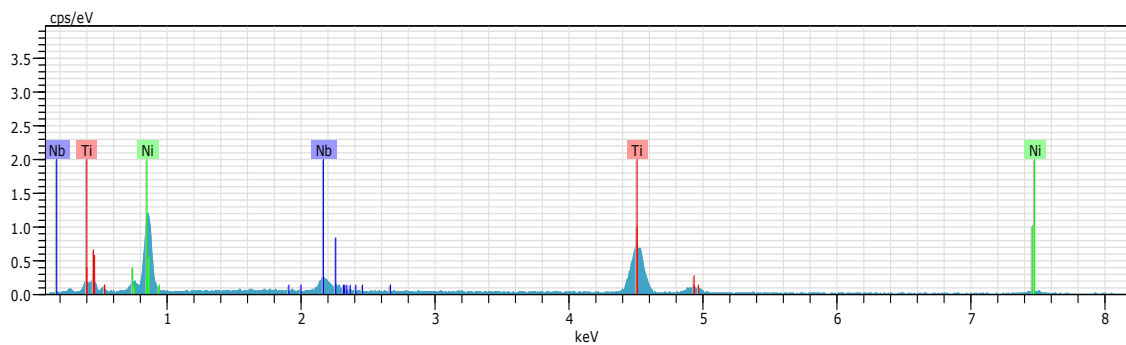


Figure 2. Cont.



| Element | Atomic% |
|---------|---------|
| Ti K    | 51.73   |
| Ni K    | 44.02   |
| Nb K    | 4.25    |
| Total   | 100.00  |

(e)



| Element | Atomic% |
|---------|---------|
| Ti K    | 49.80   |
| Ni K    | 44.25   |
| Nb K    | 5.95    |
| Total   | 100.00  |

(f)

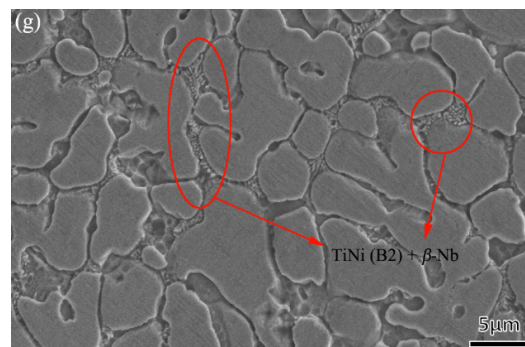


**Figure 2.** SEM surface morphologies of: (a)  $\text{TiNi}_{44}\text{Nb}_2$ , (b)  $\text{TiNi}_{44}\text{Nb}_4$ , and (c)  $\text{TiNi}_{44}\text{Nb}_6$  alloys. EDS analysis for (d)  $\text{TiNi}_{44}\text{Nb}_2$ , (e)  $\text{TiNi}_{44}\text{Nb}_4$ , and (f)  $\text{TiNi}_{44}\text{Nb}_6$  alloys, (g) the higher magnification view for (c).

### 3.3. Mechanical Properties

Figures 3–5 show the mechanical response of the TiNi<sub>44</sub>Nb<sub>2</sub>, TiNi<sub>44</sub>Nb<sub>4</sub> and TiNi<sub>44</sub>Nb<sub>6</sub> alloys, respectively, under quasi-static and dynamic compressive loads. In general, the results show that for Nb additions of less than 4 at.%, an increasing Nb content led to a higher failure stress and failure strain. In other words, the interstitial insertion of the Nb atoms prompted a distortion of the TiNi lattice, which increased the lattice strain and impeded the movement of dislocations, thereby resulting in a solid solution strengthening effect. However, as the level of Nb addition was further increased to 6 at.%, the strength decreased and the ductility increased due to the formation of a soft β-Nb phase, as shown in Figures 1 and 2.

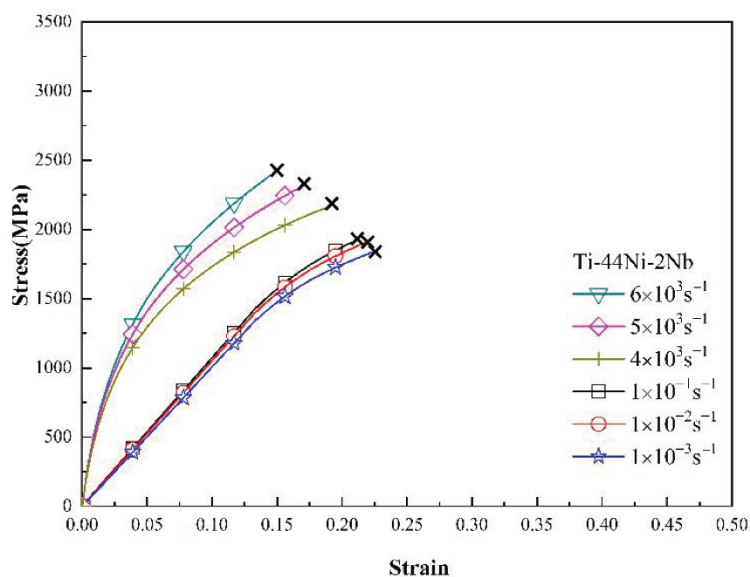


Figure 3. Low strain rate and high strain rate deformation curves of TiNi<sub>44</sub>Nb<sub>2</sub> alloy.

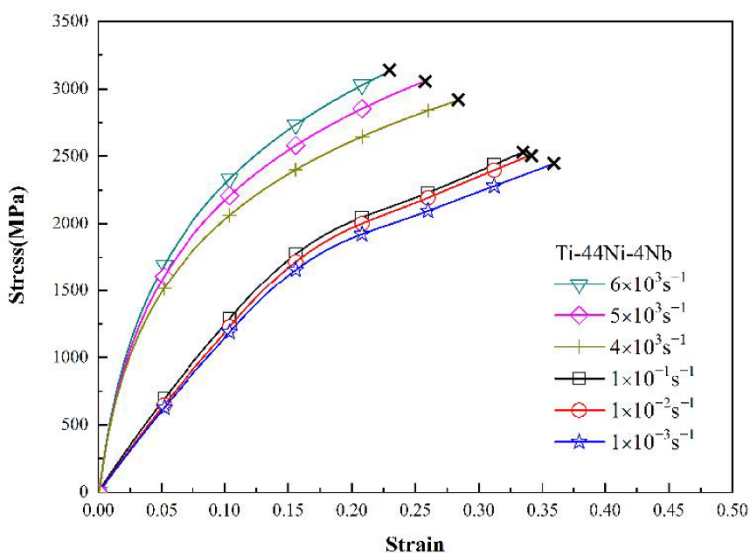


Figure 4. Low strain rate and high strain rate deformation curves of TiNi<sub>44</sub>Nb<sub>4</sub> alloy.

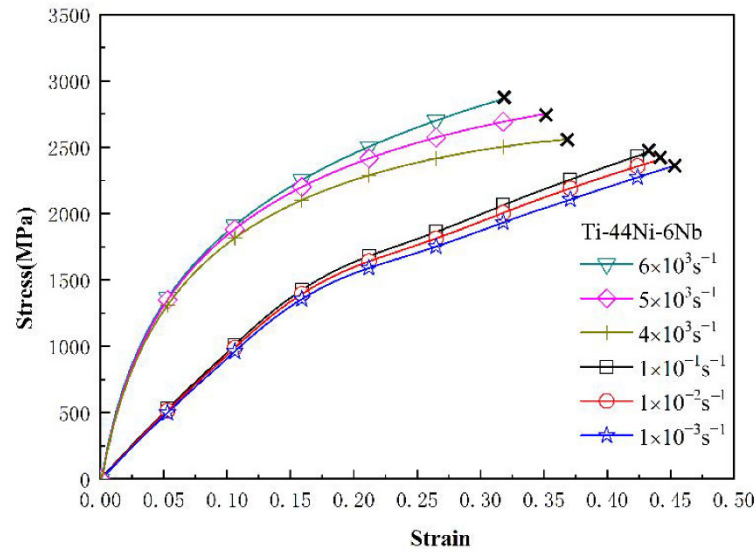


Figure 5. Low strain rate and high strain rate deformation of TiNi<sub>44</sub>Nb<sub>6</sub> alloy.

3.4. Strain Rate Sensitivity Effect

Figures 6 and 7 show the variation in the flow stress with the strain rate for the three alloys as a function of the strain under static and dynamic loading conditions, respectively. It can be seen that, for both deformation regimes, the strain rate and Nb content had a significant effect on the plastic flow stress. Moreover, for a constant strain rate, the flow stress increased with increasing strain. Among all the alloys, the TiNi<sub>44</sub>Nb<sub>4</sub> alloy exhibited the maximum plastic flow stress for all values of the strain and strain rate. The effect of the strain rate and Nb content on the mechanical response of the three alloys can be evaluated via the following strain rate sensitivity ( $\beta$ ) [35]:

$$\beta = \frac{\sigma_2 - \sigma_1}{\ln(\dot{\epsilon}_2 / \dot{\epsilon}_1)}$$

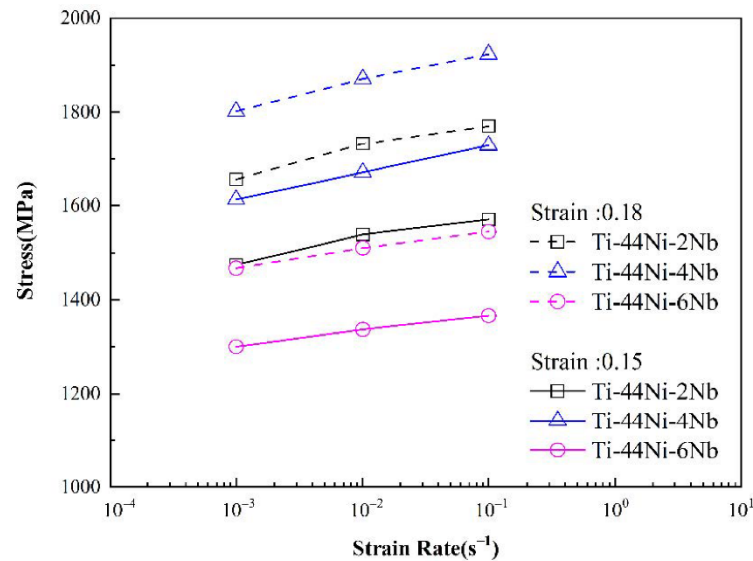


Figure 6. Variation of plastic flow stress with strain rate under static deformation conditions.

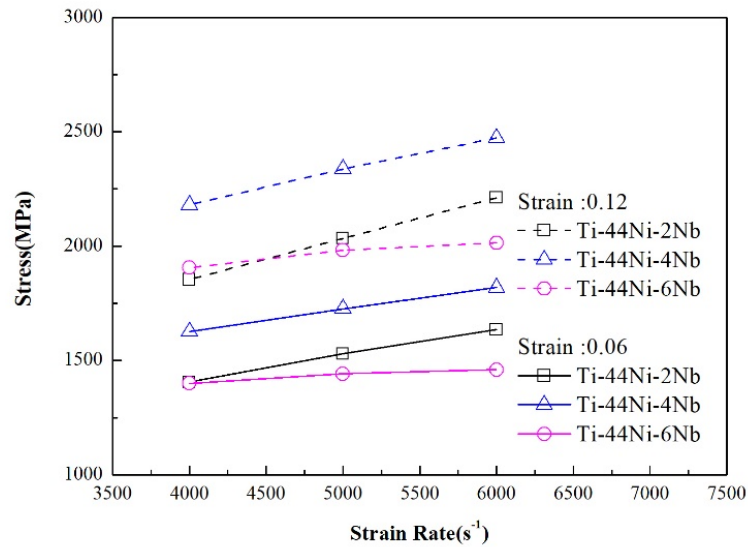


Figure 7. Variation of plastic flow stress with strain rate under dynamic deformation conditions.

Figures 8 and 9 show the variation in the strain rate sensitivity exponent with the true strain as a function of the strain rate under quasi-static and dynamic loading conditions, respectively. For both deformation regimes, and all values of the strain rate, the strain rate sensitivity increased with increasing strain. In other words, the strain rate increased with increasing strain. The maximum strain rate sensitivity occurred in the  $\text{TiNi}_{44}\text{Nb}_4$  alloy, irrespective of the loading condition (quasi-static or dynamic). Moreover, the strain rate sensitivity reduced significantly in the  $\text{TiNi}_{44}\text{Nb}_6$  specimen with 6 at.% Nb addition. It is speculated that the reduced strength and enhanced ductility of the  $\text{TiNi}_{44}\text{Nb}_6$  alloy was due to the softening effects of the  $\beta$ -Nb phase formed at the grain boundaries, as shown in Figure 2c.

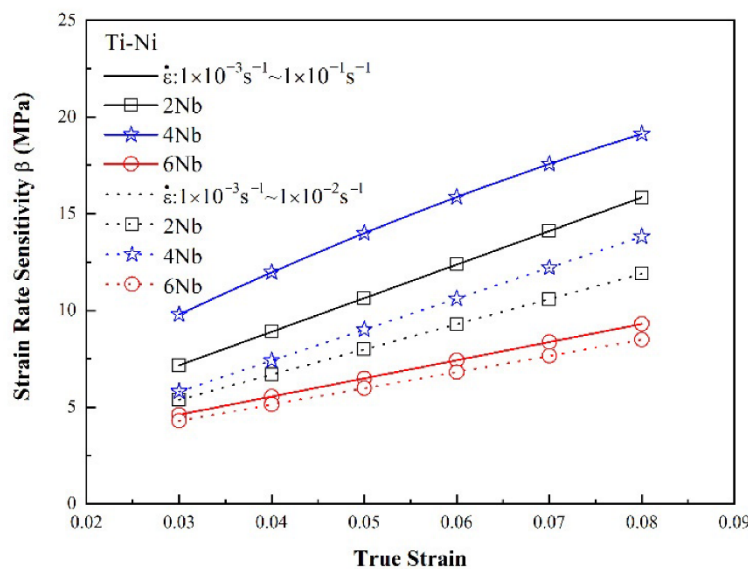
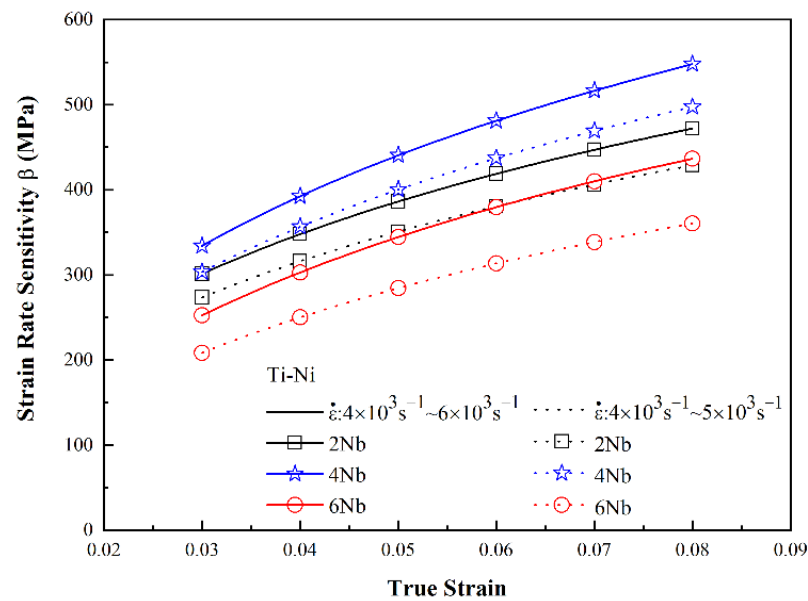


Figure 8. Strain rate sensitivity as a function of true strain under static deformation conditions.



**Figure 9.** Strain rate sensitivity as a function of true strain under dynamic deformation conditions.

### 3.5. Fracture Surface Morphology Analysis

As shown in the stress-strain curves in Section 3.3, all the specimens failed under the considered quasi-static and dynamic strain rates. To investigate the failure mode for each sample, the fracture surfaces were examined by SEM. Figure 10a,b show the fracture surface of the  $\text{TiNi}_{44}\text{Nb}_2$  alloy under quasi-static and dynamic strain rates of  $10^{-1} \text{ s}^{-1}$  and  $5 \times 10^3 \text{ s}^{-1}$ , respectively. For both strain rates, the fracture surface contained multiple fracture planes and numerous cracks at the grain boundary, which suggests that the onset of specimen failure occurred at the grain boundaries. Overall, the results show that the failure mode was one of intergranular fracture (i.e., brittle failure). For the  $\text{TiNi}_{44}\text{Nb}_4$  alloy, both fracture surfaces contained intergranular fractures and granular equiaxed dimples. In other words, the fracture surfaces showed evidence of a mixed brittle-ductile failure mode (see Figure 11). For the  $\text{TiNi}_{44}\text{Nb}_6$  alloy, the addition of a greater amount of Nb reduced the number of intergranular fracture features and increased the density (i.e., reduced the size) of the equiaxed dimples (see Figure 12). Overall, the OM images shown in Figures 10–12 indicate that the addition of 2–4 at.% Nb resulted in a grain refinement effect, which prompted solid solution strengthening of the alloy with corresponding improvement in the mechanical performance. However, for a higher level of Nb addition (6 at.%), a soft  $\beta$ -Nb phase was formed, which reduced the strength of the alloy and increased its ductility.

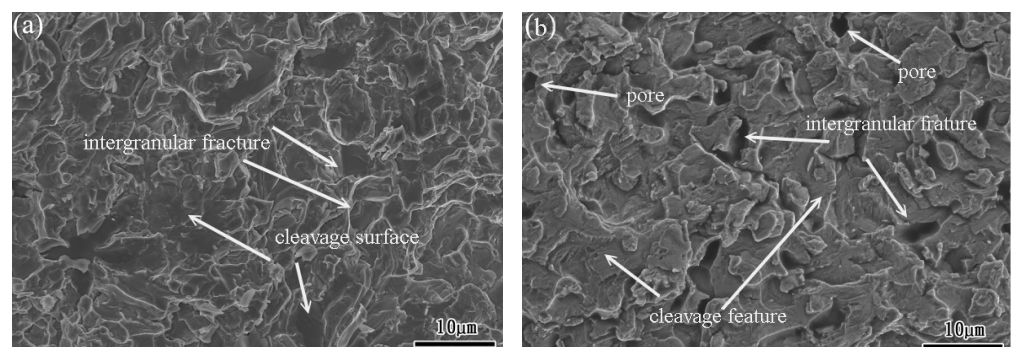


**Figure 10.** Fracture surface morphology of  $\text{TiNi}_{44}\text{Nb}_2$  alloy under (a) static deformation conditions, and (b) dynamic deformation conditions (2000× magnification).

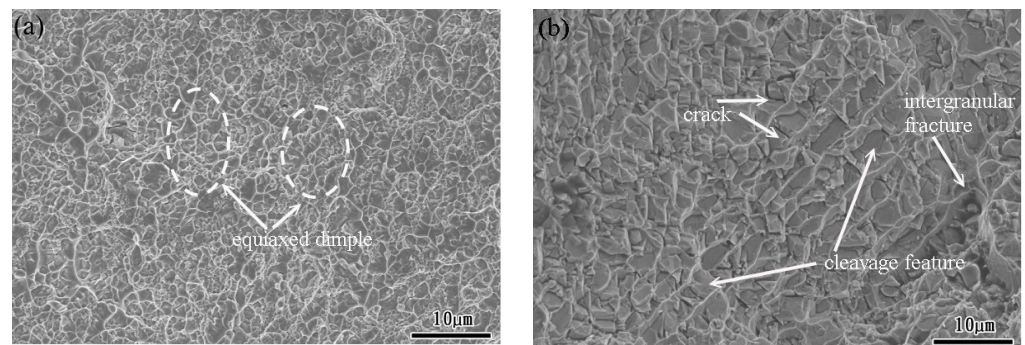


**Figure 11.** Fracture surface morphology of  $\text{TiNi}_{44}\text{Nb}_4$  alloy under (a) static deformation conditions, and (b) dynamic deformation conditions ( $2000\times$  magnification).

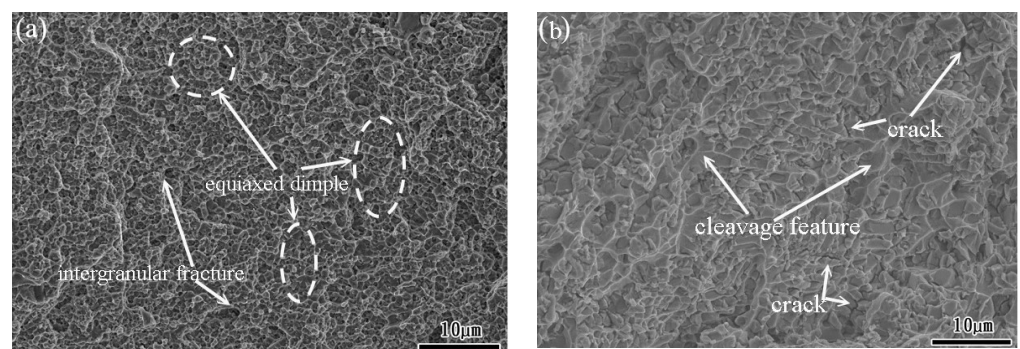


**Figure 12.** Fracture surface morphology of  $\text{TiNi}_{44}\text{Nb}_6$  alloy under (a) static deformation conditions, and (b) dynamic deformation conditions ( $2000\times$  magnification).

#### 4. Conclusions

$\text{TiNi}$  intermetallic alloys were prepared with 2, 4 and 6 at.% niobium (Nb) addition. The mechanical properties and microstructures of the alloys were investigated under both static and dynamic loading conditions. The experimental results support the following main conclusions.

1. The  $\text{TiNi}_{44}\text{Nb}_2$  and  $\text{TiNi}_{44}\text{Nb}_4$  alloys were composed principally of  $\text{TiNi}$  and  $\text{Ti}_2\text{Ni}$  phase. However, for a higher Nb addition of 6 at.%, the microstructure contained a mixture of  $\text{TiNi}$  phase and eutectic  $\text{TiNi} + \beta\text{-Nb}$  phase.
2. All the  $\text{TiNi-Nb}$  alloys had a dendritic structure. As the Nb content increased, the alloys underwent a densification of the dendritic structure and a grain refinement effect. The eutectic  $\text{TiNi} + \beta\text{-Nb}$  phase in the  $\text{TiNi}_{44}\text{Nb}_6$  alloy was located at the grain boundaries and resulted in a significant softening effect.
3. For both deformation regimes (i.e., quasi-static and dynamic), the maximum stress occurred in the  $\text{TiNi}_{44}\text{Nb}_4$  alloy.
4. As the level of Nb addition increased, the fracture mode transitioned from a predominantly brittle fracture mode (2 at.% Nb) to a mixed brittle-fracture mode (4 at.%), and finally a predominantly ductile fracture mode (6 at.%).
5. In this study, we determined that the addition of Nb to  $\text{TiNi}$  alloy could enhance the mechanical properties for engineering applications. In particular, Nb addition can enhance the ductility and strength of the high strain rate application at room temperature.

**Author Contributions:** Writing-review, methodology and editing: T.-H.C.; conceptualization, data analysis and writing—original draft preparation: H.-F.Y.; experiment: Y.-Y.S. All authors have read and agreed to the published version of the manuscript.

**Funding:** This research was funded by the Ministry of Science and Technology in Taiwan under Grant No. MOST-110-2628-E-992-002.

**Institutional Review Board Statement:** Not applicable.

**Informed Consent Statement:** Not applicable.

**Data Availability Statement:** Not applicable.

**Acknowledgments:** The authors gratefully acknowledge the financial support provided to this study by the Ministry of Science and Technology, Taiwan and National Kaohsiung University of Science and Technology.

**Conflicts of Interest:** The authors declare no conflict of interest.

## References

1. Tanaka, T.; Nezu, M.; Uchida, S.; Hirata, T. Mechanism of intermetallic compound formation during the dissimilar friction stir welding of aluminum and steel. *J. Mater. Sci.* **2020**, *55*, 3064–3072. [[CrossRef](#)]
2. Long, M.; Rack, H.J. Titanium alloys in total joint replacement—a materials science perspective. *Biomaterials* **1998**, *19*, 1621–1639. [[CrossRef](#)]
3. Sauthoff, G. Multiphase intermetallic alloys for structural applications. *Intermetallics* **2000**, *8*, 1101–1109. [[CrossRef](#)]
4. Yun, J.H.; Oh, M.H.; Nam, S.W.; Wee, D.M.; Inui, H.; Yamaguchi, M. Microalloying effects in TiAl+Mo alloys. *Mater. Sci. Eng. A* **1997**, *239–240*, 702–708. [[CrossRef](#)]
5. Kim, Y.W. Ordered intermetallic alloys, part III: Gamma titanium aluminides. *JOM* **1994**, *46*, 30–39. [[CrossRef](#)]
6. Tetsui, T. Effects of high niobium addition on the mechanical properties and high-temperature deformability of gamma TiAl alloy. *Intermetallics* **2002**, *10*, 239–245. [[CrossRef](#)]
7. Khan, A.S.; Suh, Y.S.; Kazmi, R. Quasi-static and dynamic loading responses and constitutive modeling of titanium alloys. *Int. J. Plast.* **2004**, *20*, 2233–2248. [[CrossRef](#)]
8. Lee, W.S.; Chen, C.W. Dynamic mechanical properties and microstructure of Ti-6Al-7Nb biomedical alloy as function of strain rate. *Mater. Sci. Technol.* **2013**, *29*, 1055–1064. [[CrossRef](#)]
9. Zhan, H.Y.; Wang, G.; Kent, D.; Dargusch, M. The dynamic response of a metastable  $\beta$  Ti–Nb alloy to high strain rates at room and elevated temperatures. *Acta Mater.* **2016**, *105*, 104–113. [[CrossRef](#)]
10. Tiwary, C.S.; Pandey, P.; Sarkar, S.; Das, R.; Samal, S.; Biswas, K.; Chattopadhyay, K. Five decades of research on the development of eutectic as engineering materials. *Prog. Mater. Sci.* **2022**, *123*, 100793. [[CrossRef](#)]
11. Ren, D.C.; Zhang, H.B.; Liu, Y.J.; Li, S.J.; Jin, W.; Yang, R.; Zhang, L.C. Microstructure and properties of equiatomic Ti–Ni alloy fabricated by selective laser melting. *Mater. Sci. Eng. A* **2020**, *771*, 138586. [[CrossRef](#)]
12. Liu, D.; Peterlechner, M.; Fiebig, J.; Trubel, S.; Wegner, M.; Du, Y.; Jin, Z.; Wilde, G.; Divinski, S.V. Grain boundary diffusion and precipitates in B2 Ti<sub>50.2</sub> at.% Ni alloy. *Intermetallics* **2015**, *61*, 30–37. [[CrossRef](#)]
13. Cui, B.; Yao, J.; Wu, Y.; Zhang, X.; Wang, F.; Sui, J.; Cai, W. Precipitation behavior and mechanical properties of Ti–Ni–Nb–Co alloys. *Intermetallics* **2018**, *95*, 40–47. [[CrossRef](#)]
14. Wu, S.K.; Chang, Y.C. Thermal Cycling Effect on Transformation Temperatures of Different Transformation Sequences in TiNi-Based Shape Memory Alloys. *Materials* **2019**, *12*, 2512. [[CrossRef](#)] [[PubMed](#)]
15. Basova, T.V.; Vikulova, E.S.; Dorovskikh, S.I.; Hassan, A.; Morozov, N.B. The use of noble metal coatings and nanoparticles for the modification of medical implant materials. *Mater. Des.* **2021**, *204*, 109672. [[CrossRef](#)]
16. Som, I.; Balla, V.K.; Das, M.; Sukul, D. Thermally oxidized electron beam melted  $\gamma$ -TiAl: In vitro wear, corrosion, and biocompatibility properties. *J. Mater. Res.* **2018**, *33*, 2096–2105. [[CrossRef](#)]
17. Parvizi, S.; Seyed Mahdi Hashemi, S.M.; Asgarinia, F.; Nematollahi, M.; Elahinia, M. Effective parameters on the final properties of NiTi-based alloys manufactured by powder metallurgy methods: A review. *Prog. Mater. Sci.* **2021**, *117*, 100739. [[CrossRef](#)]
18. Zhang, D.T.; Guo, B.; Tong, Y.X.; Tian, B.; Li, L.; Zheng, Y.F.; Gunderov, D.V.; Valiev, R.Z. Effect of annealing temperature on martensitic transformation of Ti<sub>49.2</sub>Ni<sub>50.8</sub> alloy processed by equal channel angular pressing. *Trans. Nonferrous Met. Soc. China* **2016**, *26*, 448–455. [[CrossRef](#)]
19. Zheng, H.X.; Mentz, J.; Bram, M.; Buchkremer, H.P.; Stöver, D. Powder metallurgical production of TiNiNb and TiNiCu shape memory alloys by combination of pre-alloyed and elemental powders. *J. Alloys Compd.* **2008**, *463*, 250–256. [[CrossRef](#)]
20. Wu, K.H.; Wang, Y.; Chou, K.C.; Zhang, G.H. Low-temperature synthesis of single-phase refractory metal compound carbides. *Int. J. Refract. Met. Hard Mater.* **2021**, *98*, 105567. [[CrossRef](#)]
21. Wang, C.; Li, B.; Xu, Q.; Wang, T.; Qi, P.; Nie, Z.R. Effect of Primary  $\alpha$  Phase Content on Creep Property of High Temperature Titanium Alloy. *Mater. Sci. Forum* **2020**, *993*, 217–222. [[CrossRef](#)]
22. Ma, L.; Zhou, C.; Shi, Y.; Cui, Q.; Ji, S.; Yang, K. Grain-Refinement and Mechanical Properties Optimisation of A356 Casting Al by Ultrasonic-Assisted Friction Stir Processing. *Met. Mater. Int.* **2021**, *27*, 5374–5388. [[CrossRef](#)]
23. Li, W.; Wu, Y.; Wu, Y.; Li, Y.; Ehti, A.; Liu, X. Duplex Nucleation and Its Effect on the Grain Size and Properties of Near Eutectic Al–Si Alloys. *Materials* **2022**, *15*, 2507. [[CrossRef](#)]

24. Lee, C.; Chou, Y.; Kim, G.; Gao, M.C.; An, K.; Brechtel, J.; Zhang, C.; Chen, W.; Poplawsky, J.D.; Song, G.; et al. Lattice-Distortion-Enhanced Yield Strength in a Refractory High-Entropy Alloy. *Adv. Mater.* **2020**, *32*, 2004029. [[CrossRef](#)] [[PubMed](#)]
25. Wang, Q.; Sun, Y.; Zhang, C.; Wang, Q.; Zhang, F. Effect of Nb on microstructure and yield strength of a high temperature tempered martensitic steel. *Mater. Res. Express* **2018**, *5*, 046501. [[CrossRef](#)]
26. Huang, S.; Wu, H.; Zhu, H.; Xie, Z. Effect of niobium addition upon microstructure and tensile properties of CrMnFeCoNi<sub>x</sub> high entropy alloys. *Mater. Sci. Eng. A* **2021**, *809*, 140959. [[CrossRef](#)]
27. Artyukhova, N.; Anikeev, S.; Promakhov, V.; Korobekov, M. The Effect of Cobalt on the Deformation Behaviour of a Porous TiNi-Based Alloy Obtained by Sintering. *Materials* **2021**, *14*, 7584. [[CrossRef](#)] [[PubMed](#)]
28. Lin, C.W.; Ju, C.P.; Lin, J.-H.C. A comparison of the fatigue behavior of cast Ti-7.5Mo with c.p. titanium, Ti-6Al-4V and Ti-13Nb-13Zr alloys. *Biomaterials* **2005**, *26*, 2899–2907. [[CrossRef](#)]
29. Cvijović-Alagić, I.; Cvijović, Z.; Mitrović, S.; Panić, V.; Rakin, M. Wear and corrosion behaviour of Ti-13Nb-13Zr and Ti-6Al-4V alloys in simulated physiological solution. *Corros. Sci.* **2011**, *53*, 796–808. [[CrossRef](#)]
30. Niinomi, M. Mechanical properties of biomedical titanium alloys. *Mater. Sci. Eng. A* **1998**, *243*, 231–236. [[CrossRef](#)]
31. Zheng, L.J.; Zhang, F.X.; Ding, R.G.; Wang, E.F.; Zhang, H. New phase and deformation behavior in directional solidified NiTiAl based intermetallic alloy upon cyclic tensile loading-unloading. *Mater. Des.* **2016**, *110*, 494–502. [[CrossRef](#)]
32. Xiao, F.; Ma, G.; Zhao, X.; Xu, H. Effects of Nb Content on Yield Strength of NiTiNb Alloys in Martensite State. *Chin. J. Aeronaut.* **2019**, *22*, 658–662. [[CrossRef](#)]
33. Fan, Q.C.; Zhang, Y.; Zhang, Y.H.; Wang, Y.Y.; Yan, E.H.; Huang, S.K.; Wen, Y.H. Influence of Ni/Ti ratio and Nb addition on martensite transformation behavior of NiTiNb alloys. *J. Alloys Compd.* **2019**, *790*, 1167–1176. [[CrossRef](#)]
34. Dagdelen, F.; Balci, E.; Qader, I.N.; Ozen, E.; Kok, M.; Kanca, M.S.; Abdullah, S.S.; Mohammed, S.S. Influence of the Nb Content on the Microstructure and Phase Transformation Properties of NiTiNb Shape Memory Alloys. *JOM* **2020**, *72*, 1664–1672. [[CrossRef](#)]
35. Andrade, U.R.; Meyers, M.A.; Chokshi, A.H. Constitutive description of work-and shock-hardened copper. *Scripta Metal. Mater.* **1994**, *30*, 933–938. [[CrossRef](#)]